

Efficient Time Series Forecasting via Hyper-Complex Models and Frequency Aggregation

Eyal Yakir, Dor Tsur, and Haim Permuter
 School of Electrical and Computer Engineering
 Ben-Gurion University of the Negev, Be'er Sheva, Israel
 {eyalyak, dortz}@post.bgu.ac.il, haimp@bgu.ac.il

Abstract

Time series forecasting is a long-standing problem in statistics and machine learning. One of the key challenges is processing sequences with long-range dependencies. To that end, a recent line of work applied the short-time Fourier transform (STFT), which partitions the sequence into multiple subsequences and applies a Fourier transform to each separately. We propose the Frequency Information Aggregation (FIA)-Net, which is based on a novel complex-valued MLP architecture that aggregates adjacent window information in the frequency domain. To further increase the receptive field of the FIA-Net, we treat the set of windows as hyper-complex (HC) valued vectors and employ HC algebra to efficiently combine information from all STFT windows altogether. Using the HC-MLP backbone allows for improved handling of sequences with long-term dependence. Furthermore, due to the nature of HC operations, the HC-MLP uses up to three times fewer parameters than the equivalent standard window aggregation method. We evaluate the FIA-Net on various time-series benchmarks and show that the proposed methodologies outperform existing state of the art methods in terms of both accuracy and efficiency. Our code is publicly available on <https://anonymous.4open.science/r/research-1803/>.

1 Introduction

Time series forecasting (TSF) is a long standing challenge, which plays a key role in various domains, such as energy management [1], traffic prediction [2] and financial analysis [3]. With the development of deep learning, myriad neural network (NN) architectures had been proposed, and have gradually improved the accuracy on the TSF problem. Two key architectures has been used for TSF are recurrent NNs (RNNs) [4, 5, 6] and transformers [7, 8, 9, 10], each of which aims to capture long-term dependencies through a different functional feature extraction procedure. While both methods were proven useful, RNNs struggled with long-term dependencies [11] or non-stationary data patterns, While transformer architectures may overlook important temporal information due to permutation invariance [12], they require many parameters and may suffer from long runtime. Additional NN-based approaches for TSF consider graph NNs (GNNs) [13] and decomposition models [14].

Recent advancements have demonstrated promising results in processing and extracting features from the frequency domain [15]. Techniques leveraging frequency-based transformations have been in various contexts, ranging from computational efficiency improvements [9] to seasonal-trend decomposition [8]. To better process the frequency domain data, [16]

developed a complex-valued MLP, which demonstrated superior capability in capturing both temporal and cross-channel dependencies. To better handle nonstationarities in the data, [17] substituted the standard FFT with the Short-Time Fourier Transform (STFT) [18], which divides the sequence into separate windows and transforms each window individually into the frequency domain. While showing better suitability for non-stationary time series data, the STFT yields a set of windows, each of which represents exclusive information on the sequence. However, in practice, adjacent windows are highly correlated, albeit processed separately by current STFT-based models.

To incorporate the overlooked shared information, we propose the FIA-Net, a novel TSF model that is designed to handle long-term dependencies in the data by aggregating information from subsets of STFT windows. The FIA-Net has an MLP backbone that processes the STFT windows in the frequency domain. We propose two novel MLP architectures. The first, is termed window-mixing MLP (WM-MLP), which mixes each STFT windows with its neighboring bands. The second is the HC-MLP. The HC-MLP leverages HC algebra to efficiently combine information from *all* STFT together. By using HC algebra, the STFT implements with three times less parameters than the equivalent WM-MLP.

The main contributions of this paper are as follows

- We construct the FIA-Net and the WM-MLP backbone. The resulting TSF model captures inter-window dependencies in the frequency domain and benefits from a forward pass complexity of $O(L \log L/p)$ operations, where L is the lookback window length and p is the number of STFT windows.
- We propose a novel HC-MLP backbone that expands the receptive field of the WM-MLP, while requiring a fraction of total parameters.
- To reduce the model size and complexity, we filter the STFT windows, leaving only the top- M frequency components. We show that accuracy is maintained even when M is significantly smaller than the total number of components.
- We provide an array of experiments that demonstrate the performance of the model and its efficiency. We show that the FeeqShiftNet improves upon existing models accuracy by up to 20%.
- We provide an ablation study, in which explores the effect of operating over the complex plane and compare the performance of the two considered MLP backbones.

2 Related Work

Time-Series Forecasting The first notable works on TSF utilize classical statistical linear models such as ARIMA [19, 20] which consider series decomposition. Those were then generalized to a non-linear setting in [21]. To overcome the limitations posed by the classical models, deep learning was incorporated, where initially, sequential deep learning was performed by RNN-based models. Two key RNN models are long-short term memory networks [5] which introduce a sophisticated gating mechanism and the DeepAR model [4] that connected the RNN model with AR modeling. Despite their expressive power for sequential modeling, RNN demonstrated low efficiency and introduced high runtimes in

both the forward and backward pass [11]. Two popular architectures were proposed to improve upon RNNs; transformers and GNNs. Notable transformer-based methods are Informer [22], Reformer [23], and PatchTST [24], each leveraging the attention mechanism to capture temporal dependencies, while proposing sophisticated methods to reduce the attention operation complexity. GNNs, however, allowed for better modeling of dependencies between time series variables by treating them as graph nodes, making them particularly suitable for capturing spatio-temporal patterns. For example, AGCRN [25] introduced an adaptive graph convolution mechanism to dynamically adjust the graph structure based on inter-series relationships, while MTGNN [13] combined graph convolutions with temporal convolutional layers to jointly learn spatial-temporal dependencies.

Frequency Domain Models for Time Series Forecasting A recent line of work attempts to solve the TFS problem in the frequency domain [15], with the purpose of revealing patterns that may be hidden in the time domain. The FEDformer [8] uses a Fourier-based framework to separate trend and seasonal components by leveraging the Fourier Transform on sub-sequences, allowing it to isolate periodic patterns more effectively. ETSformer [26] combines exponential smoothing and applies attention in the frequency domain to enhance seasonality modeling by capturing both short- and long-term dependencies. In FiLM [27], Fourier projections are used to reduce noise and emphasize relevant features. Additionally, SFM [28] and StemGNN [29] utilize frequency decomposition and Graph Fourier Transforms to handle complex temporal dependencies in multivariate time series. FRETTS [16] extends this approach by proposing frequency-domain MLPs to learn complex relationships between real and imaginary components of the FFT. FREQTSF [17] uses STFT with attention mechanisms to capture temporal patterns across overlapping time windows. While frequency models, and specifically the recent use of STFT, have shown significant improvement in TFS performance, each STFT window is often processed separately, ignoring the strong correlations between adjacent windows.

Hyper-complex Numbers HC numbers extend the complex number system to higher dimensions [30]. Base-4 HC numbers, have been widely used in computer graphics to model 3D rotations [31]. Base-8 HC numbers have been explored in image classification and compression [31, 32], developing an HC network that showed favorable performance on popular datasets. The merit of HC numbers to extract relevant information in time-series was explored in [33], in which an HC-net was used to analyse brain-wave data, and in [34], which explored HC-network for financial data. In this work, we explore the utility of HC architectures for the efficient processing of STFT windows in the frequency domain.

3 Proposed Model : FIA-Net

In this section, we describe FIA-Net, a TSF model that leverages shared information between STFT windows. We begin by discussing the existing gap in current frequency domain TSF methods, followed by a brief introduction to frequency domain MLPs [35]. We then outline the FIA-Net components, presenting the novel complex MLP backbone, discussing a simple frequency compression step that reduces the MLP input dimension, and outline the complete model.

Motivation

Even though most real-world time-series data is nonstationary, it may adhere to a piecewise

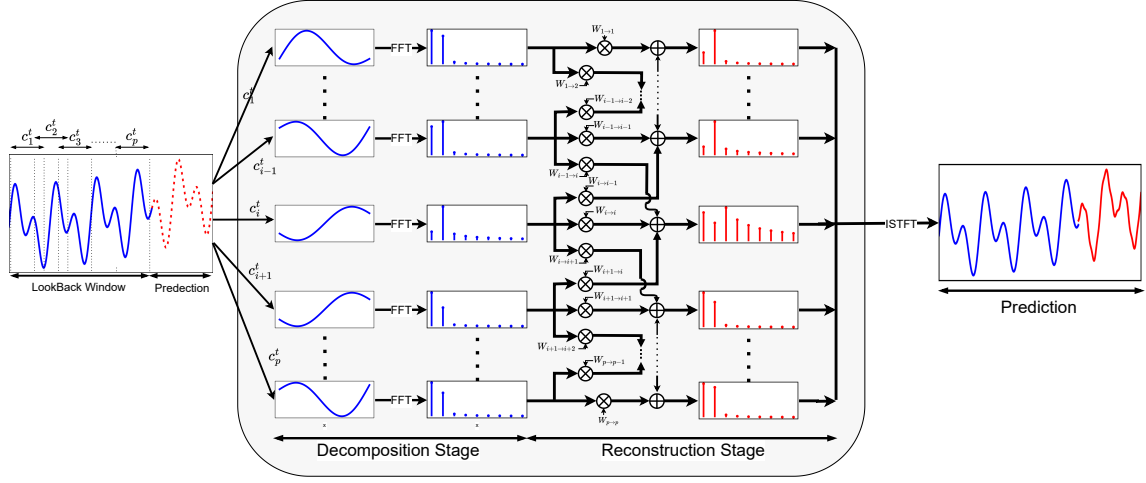


Figure 1: Window Mixing mechanism. An input X is transformed into a set of p STFT windows which are transformed to the frequency domain and are then fed into the WM-MLP, which aggregates adjacent windows. The WM-MLP outputs are then transformed back to the time domain via a real STFT, from which the prediction (red) is obtained.

stationary structure, as observed in speech signals [36] and financial data [37]. This local stationarity allows us to partition the series into stationary correlated STFT subsequences that can be transformed in the frequency domain. The correlation between the STFT sequences has been efficiently utilized in recent works, even though, as we later show, it affects the downstream model accuracy in the task of time prediction.

Frequency Domain MLPs

As we handle complex-valued data, we adopt the frequency domain MLP (FD-MLP) unit from [16]. The FD-MLP generalizes the simple neuron to operate with complex-valued weights and biases. Incorporating complex MLPs has been shown to improve the model performance as it aligns better with the geometrical structure induced by the complex plane. The FD-MLP unit is visualized in Figure 2. In Section 4, we will discuss the expansion of the FD-MLP for hyper-complex numbers.

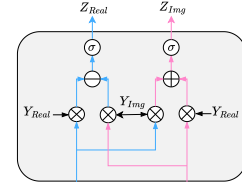


Figure 2: FD-MLP architecture.

3.1 Adjacent Information Aggregation

Consider a sequence $X = \{x_1, \dots, x_L\} \in \mathbb{R}^{D \times L}$ where $x_i \in \mathbb{R}^D$, L is the sequence length, which we refer to as the lookback size, and D is the latent space dimension. Our objective is to predict the next T elements of the sequence $\hat{X} = \{\hat{x}_{L+1}, \dots, \hat{x}_{L+T}\} \in \mathbb{R}^{D \times T}$, where T is a predetermined prediction horizon. We are interested in processing X in the frequency domain. We utilize the STFT, which partitions X into p windows and applies the FFT separately to each window. In addition, we exploit the real-valued inputs to perform a Real STFT, which

results in half the frequency coefficients. The STFT for the i -th window is defined as:

$$\text{STFT}\{X\}(\omega, \tau_i) = \sum_{t=1}^L x_t w(t - \tau_i) e^{-j\omega t}, \quad (1)$$

Where, $w(t - \tau_i)$ is the window function centered at the location of the i -th window ($i \in \{1, \dots, p\}$), ω represents the angular frequency, and j satisfies $j^2 = -1$. Each window is defined by its center τ_i and has a size of $\frac{N_{\text{FFT}}}{2} + 1$. The output of the STFT consists of p windows, each producing a spectrum of length $\frac{N_{\text{FFT}}}{2} + 1$. We propose the window mixing MLP (WM-MLP), which adapts the FD-MLP to properly aggregate neighboring STFT windows to incorporate shared information. Given a set of complex transformed windows $\{C_1, \dots, C_p\}$, the WM-MLP operates on the i th window C_i^{in} as follows:

$$C_i^{\text{out}} = \sigma(C_i^{\text{in}} W_{i \rightarrow i} + C_{i-1}^{\text{in}} \overline{W}_{(i-1) \rightarrow i} + C_{i+1}^{\text{in}} \overline{W}_{(i+1) \rightarrow i} + B_i) \quad (2)$$

where $\sigma(\cdot)$ is an activation function, $(W_{(i-1) \rightarrow i}, W_{i \rightarrow i}, W_{(i+1) \rightarrow i})_{i=1}^p$ are the WM-MLP weight matrices with C_j being a matrix of zeros for $j \notin \{1, \dots, p\}$, and $(B_i)_{i=1}^p$ are the WM-MLP bias vectors, and \overline{W} is the elementwise complex conjugate of W . The outputs of the WM-MLP are transformed back to the time domain using the element-wise inverse STFT, which is given by:

$$\text{iSTFT}\{X^F(w, \tau_i)\}(t) = \sum_{\omega} X^F(\omega, \tau) e^{j\omega t} w(t - \tau_i) \quad (3)$$

The STFT, WM-MLP operation, and inverse transform are depicted by Figure 1. In highly nonstationary data, energy transition between adjacent windows can be sharp. To that end, we introduce a minor overlap between adjacent windows of $N_{\text{FFT}} - \frac{L - N_{\text{FFT}}}{p-1}$, which implicitly adjusts their statistics prior to processing by the TSF model by increasing the inter-window correlations.

3.2 Implementation Details and Complete System

Selective Frequency Compression To reduce the input dimensionality to the WM-MLP, we compress each transformed window $C_i \in \mathbb{C}^{N_{\text{FFT}} \times D}$ along the frequency axis. Specifically, we select the top M frequency components based on their real and imaginary values across each dimension and denote the compressed window with C_i^M . Then, (C_1^M, \dots, C_p^M) is fed into the WM-MLP layer. The top- M procedure is given by

$$C_i^M = \underset{j=1, \dots, M}{\text{Top-M}} |C_{i,j}|_{\mathbb{C}} \quad (4)$$

where $C_{i,j}$ is the j th component of C_i and $|z|_{\mathbb{C}}$ is the magnitude of $z \in \mathbb{C}$. Additionally, we store the top component indices of (4) in a list $\mathcal{I}(i)$, which encodes the band from which the information came. To transform the WM-MLP output C_i^{out} back to the time domain, we perform a *position-aware* zero padding, which adds $N_{\text{FFT}} - M$ zeros while placing the nonzero components in their original indices, which correspond to the original frequency bands, i.e.,

$$C_{i,j}^{\text{padded}} = \begin{cases} C_{i,j}^{\text{out}}, & j \in \mathcal{I}(i) \\ 0, & \text{else.} \end{cases}$$

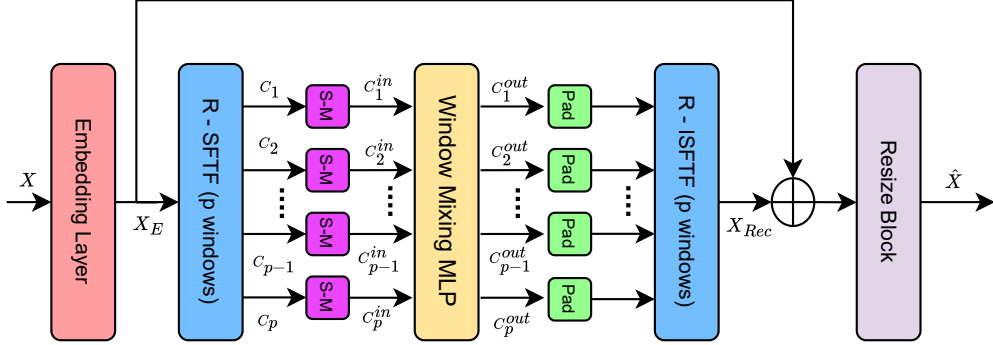


Figure 3: FIA-Net Model: The input, denoted X , is first fed into the embedding layer, resulting in X_E , which is transformed to the frequency domain via the STFT. We then extract the top- M components of each STFT window and feed the compressed windows through the WM-MLP. The MLP outputs are then passed through position-aware zero padding, whose outputs are transformed back to the time domain and summed with X_E via skip connection. The model output \hat{X} is then given by applying a linear transformation.

In Section 5, we demonstrate that, in addition to improving computational efficiency, this frequency compression procedure enhances the performance of downstream TSF tasks. The selection of top- M components allows us to reduce the model’s complexity while maintaining the most relevant frequency information.

Complete Model The complete FIA-Net, as shown in Figure 3, operates as follows: Given an input $X \in \mathbb{R}^{B \times L \times D}$, the dimension of X is expanded through a learned embedding layer, resulting in $X_E \in \mathbb{R}^{B \times L \times D \times E}$. This expanded representation is then fed into an STFT block that uses the real input to perform R – STFT on X_E . The transformed signal is passed through the SM block, whose output is further processed by the WM-MLP. The WM-MLP outputs are subsequently padded and transformed back to the temporal axis, where they are integrated with X_E via a skip connection and resized to the desired output sequence shape using a two-layer MLP decomposition.

Model Complexity The forward pass complexity of the WM-MLP is primarily determined by the STFT complexity, which is $O(L \log(\frac{L}{p}))$. This represents a significant reduction in complexity compared to transformer-based methods, which employ intricate mechanisms to reduce their $O(L^2)$ attention complexity to $O(L \log L)$. Additionally, the application of top- M frequency selection further optimizes the forward pass in the frequency domain, reducing both computational demands and the corresponding MLP size. A detailed analysis of these complexities is provided in Table 11.

4 Window Aggregation via Hyper-Complex Models

Even though the WM-MLP backbone integrates valuable information that benefits the FIA-Net’s accuracy, information is not only shared between two adjacent STFT windows. In fact, the stronger the dependencies on the long-term past, the more information is shared between two distant windows on the frequency axis. Ideally, we would like to aggregate information

between all p STFT windows. Unfortunately, a straightforward extension of the WM-MLP requires $O(p^2)$ weight matrices, which may impair the training procedure and increase model complexity. To address that, we interpret the set of windows as an HC vector and propose an HC-based MLP that efficiently processes the set of STFT windows. We begin with a short introduction on HC-algebras, followed by the construction of the proposed MLP backbone for the FIA-Net.

4.1 Hyper-complex Numbers

HC numbers generalize the complex field by introducing additional dimensions while maintaining algebraic properties. HC number systems are defined by a parameter q that determines the number of components in the number system. Complex numbers can thus be viewed as an HC number with $q = 2$, and an HC number of base q can be represented with $p = q/2$ complex numbers. In what follows, we focus on HC numbers with $p = 4$, termed Octonions \mathbb{O} , whose elements are denoted $o = (\alpha_1, \alpha_2, \alpha_3, \alpha_4) \in \mathbb{O}$, with $\alpha_i \in \mathbb{C}$ for $i = 1, \dots, 4$. Additional discussion on $p \neq 4$ is given in Appendix C.

The addition of two Octonions, $o_1 = (\alpha_1, \dots, \alpha_4)$ and $o_2 = (\beta_1, \dots, \beta_4)$, is given by their componentwise sum, while their multiplication follows the Cayley-Dickson construction [38]. The product $o_3 = o_1 \cdot o_2 = (\gamma_1, \gamma_2, \gamma_3, \gamma_4)$ is given by:

$$\begin{aligned}
 \gamma_1 &= \alpha_1\beta_1 - \alpha_2\bar{\beta}_2 - \alpha_3\bar{\beta}_3 - \alpha_4\bar{\beta}_4 \\
 \gamma_2 &= \alpha_2\bar{\beta}_1 + \alpha_1\beta_2 + \alpha_3\bar{\beta}_4 - \alpha_4\bar{\beta}_3 \\
 \gamma_3 &= \alpha_3\bar{\beta}_1 + \alpha_4\bar{\beta}_2 + \alpha_1\beta_3 - \alpha_2\bar{\beta}_4 \\
 \gamma_4 &= \alpha_4\bar{\beta}_1 + \alpha_2\bar{\beta}_3 + \alpha_1\beta_4 - \alpha_3\bar{\beta}_2
 \end{aligned} \tag{5}$$

Hyper-complex numbers exhibit additional properties such as closed-form expressions for norm calculations and norm preservation for specific bases. For completeness, we provide additional information on HC-numbers in Appendix C, where the proposed MLP is presented under specific bases.

4.2 Hyper-Complex MLP

The longer the range of temporal dependencies in the data, the more shared information there is between gathered windows. In such cases, the WM-MLP, which incorporates short-term information in the frequency domain, might fail to capture long-term dependencies. To that end, our goal is to increase the extent to which information is shared across the STFT windows. To derive a parameter-efficient solution, we incorporate HC algebra into the frequency domain learning procedure.

Assume that we are given $p = 4$ complex-valued STFT windows $(C_i^{\text{in}} \in \mathbb{C}^{B \times M \times E})_{i=1}^4$, where the second axis is the transformed frequency domain after top- M frequency component selection. We treat the set of windows as a single Octonion tensor $(C_1^{\text{in}}, C_2^{\text{in}}, C_3^{\text{in}}, C_4^{\text{in}}) \in \mathbb{O}^{B \times M \times E}$ and feed it through an HC-valued MLP, whose output is $C^{\text{out}} = \sigma(C^{\text{in}} \cdot W + B)$. For

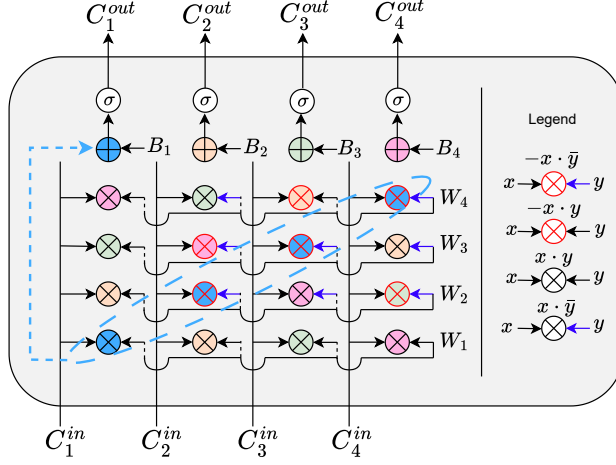


Figure 4: HC-MLP operating on $C^{\text{in}} = (C_1^{\text{in}}, C_2^{\text{in}}, C_3^{\text{in}}, C_4^{\text{in}})$, implementing the HC multiplication ((6)). Each output unit is the sum of the corresponding inner blocks of the same color, where a \oplus symbol denotes complex addition and a \otimes denotes complex multiplication. A red outline denotes minus multiplication, and a blue input arrow denotes complex conjugation.

$C^{\text{out}} = (C_1^{\text{out}}, C_2^{\text{out}}, C_3^{\text{out}}, C_4^{\text{out}})$, it is given by:

$$\begin{aligned}
C_1^{\text{out}} &= \sigma(C_1^{\text{in}}W_1 - C_2^{\text{in}}\bar{W}_2 - C_3^{\text{in}}\bar{W}_3 - C_4^{\text{in}}\bar{W}_4 + B_1), \\
C_2^{\text{out}} &= \sigma(C_2^{\text{in}}\bar{W}_1 + C_1^{\text{in}}W_2 - C_4^{\text{in}}\bar{W}_3 + C_3^{\text{in}}\bar{W}_4 + B_2), \\
C_3^{\text{out}} &= \sigma(C_3^{\text{in}}W_1 + C_1^{\text{in}}\bar{W}_3 - C_2^{\text{in}}\bar{W}_4 + C_4^{\text{in}}\bar{W}_2 + B_3), \\
C_4^{\text{out}} &= \sigma(C_4^{\text{in}}\bar{W}_1 + C_1^{\text{in}}W_4 - C_3^{\text{in}}\bar{W}_2 + C_2^{\text{in}}\bar{W}_3 + B_4).
\end{aligned} \tag{6}$$

where $W = (W_1, \dots, W_4) \in \mathbb{O}^{E \times E}$, $B = (B_1, \dots, B_4) \in \mathbb{O}^{E \times 1}$ are the HC-MLP weights and bias, respectively, and σ is a standard activation function, e.g., ReLU. We stress that, as considered in the complex MLP from [16], the HC-MLP is implemented with real-valued operations, which allows it to plug into every existing automatic differentiation scheme over standard GPUs. The HC-MLP unit is depicted in Figure 4.

The WM-MLP demonstrates distinct advantages depending on the prediction horizon. For shorter prediction lengths, it achieves better performance by effectively leveraging all available information from adjacent and nearby windows. In contrast, for longer horizons, where only closer temporal information remains relevant, the WM-MLP's ability to aggregate adjusted windows proves to be more effective. This behavior is clearly demonstrated in Section 5.2. Moreover, the HC perspective offers a significant advantage in terms of parameter efficiency. It allows for an implementation with only p weight matrices, whereas the corresponding WM-MLP would require $3p - 2$ weight matrices (and even p^2 weight matrices for a generalization of the WM-MLP), all while preserving performance. This reduction in parameters becomes increasingly dramatic as $p > 4$, as further detailed in Appendix C.

5 Results and Discussion

5.1 Experimental Setting

Datasets Following [8, 16], we consider the following representative real-world datasets: **1) WTH** (Weather), **2) Exchange** (Finance), **3) Traffic**, **4) ECL** (Electricity), **5) ETTh1** (Electricity transformer temperature hourly), and **6) ETTm1** (Electricity transformer temperature minutely). The train/validation/test split is 70%, 15%, and 15%, respectively.

Baselines In this research, we followed the TSF SoTA baselines: **1) FedFormer** [8], **2) Reformer** [23], **3) FreTS** [16], **4) PatchTST** [24], **5) Informer** [22], **6) Autoformer** [9] and **7) LSTF-Linear** [39].

Experiments setup All experiments were conducted using PyTorch [40] on a single RTX 3090, utilizing mean squared error (MSE) loss and the Adam optimizer [41]. We established an initial learning rate of 10^{-3} with an exponential decay scheduler. Hyperparameters were optimized individually for each dataset (see Appendix B.3 for specific details). We report performance metrics under both root mean squared error (RMSE) and mean absolute error (MAE). Additional information on the Normalization B.5, datasets B.1, and baseline models B.2 can be found in the appendix.

5.2 Main results

Table 1 compares the FIA-Net performance under both the WM-MLP and the HC-MLP backbones with the SoTA baselines. It is evident that the FIA-Net consistently outperforms the baselines on most considered values of prediction horizon T , with an average improvement of 5.4% in MAE and 3.8% in RMSE over SoTA models. We note that the performance of the HC-MLP-based network, which is implemented with significantly fewer parameters, achieves comparable results with the corresponding WM-MLP and attains the best results over several settings. We can deduce that the HC-MLP is more suitable for shorter-term prediction, while the WM-MLP backbone is more suitable for longer ranges.

Table 1: Forecasting performance comparison across datasets and prediction horizons using RMSE and MAE. Lower values indicate better performance. Bold denotes the best results, and underlined indicates the second-best.

	Metric	Weather				Exchange				Traffic				Electricity				ETTh1				ETTm1			
		96	192	336	720	96	192	336	720	96	192	336	720	96	192	336	720	96	192	336	720	96	192	336	720
HC-MLP (Ours)	RMSE	0.069	0.079	<u>0.090</u>	<u>0.098</u>	<u>0.050</u>	<u>0.062</u>	<u>0.078</u>	0.112	0.032	<u>0.034</u>	<u>0.035</u>	0.036	0.070	0.068	0.071	<u>0.077</u>	0.083	0.085	0.094	0.101	0.074	0.082	0.089	<u>0.096</u>
	MAE	0.030	0.039	0.043	<u>0.054</u>	<u>0.035</u>	<u>0.049</u>	<u>0.061</u>	0.089	0.016	<u>0.017</u>	<u>0.017</u>	0.018	<u>0.040</u>	<u>0.041</u>	<u>0.044</u>	0.049	0.057	0.064	0.068	0.075	0.049	<u>0.056</u>	<u>0.060</u>	<u>0.067</u>
WM-MLP (Ours)	RMSE	<u>0.071</u>	<u>0.081</u>	0.089	0.097	0.048	0.060	0.076	0.107	<u>0.033</u>	0.033	0.034	0.036	<u>0.067</u>	0.068	<u>0.070</u>	0.076	<u>0.084</u>	<u>0.088</u>	0.097	<u>0.102</u>	<u>0.076</u>	0.082	0.089	0.094
	MAE	<u>0.031</u>	<u>0.041</u>	<u>0.045</u>	0.053	0.034	0.047	0.058	0.086	0.016	0.016	0.016	0.018	0.039	<u>0.041</u>	<u>0.044</u>	0.049	0.057	0.066	0.071	0.075	<u>0.052</u>	0.055	0.058	0.064
FreTS	RMSE	<u>0.071</u>	<u>0.081</u>	<u>0.090</u>	0.099	0.051	0.067	0.082	<u>0.110</u>	0.036	0.038	0.038	<u>0.039</u>	0.065	0.064	0.072	0.079	0.087	0.091	<u>0.096</u>	0.108	0.077	<u>0.083</u>	0.089	<u>0.096</u>
	MAE	<u>0.032</u>	<u>0.040</u>	<u>0.046</u>	<u>0.055</u>	<u>0.037</u>	0.050	0.062	<u>0.088</u>	<u>0.018</u>	0.020	0.019	<u>0.020</u>	0.039	0.040	<u>0.046</u>	<u>0.052</u>	0.061	<u>0.065</u>	<u>0.07</u>	0.082	0.052	<u>0.057</u>	<u>0.062</u>	<u>0.069</u>
PatchTST	RMSE	0.074	0.084	0.094	0.102	0.052	0.074	0.093	0.166	0.032	0.035	0.039	0.040	<u>0.067</u>	<u>0.066</u>	0.067	0.081	0.091	0.094	0.099	0.113	0.082	0.085	<u>0.091</u>	0.097
	MAE	0.034	0.042	0.049	0.056	0.039	0.055	0.071	0.132	0.016	0.018	0.020	0.021	<u>0.041</u>	<u>0.042</u>	0.043	0.055	0.065	0.069	0.073	0.087	0.055	0.059	0.064	0.070
LTSF-Linear	RMSE	0.081	0.089	0.098	0.106	0.052	0.069	0.085	0.116	0.039	0.042	0.040	0.041	0.075	0.070	0.071	0.080	0.089	0.094	0.097	0.108	0.080	0.087	0.093	0.099
	MAE	0.040	0.048	0.056	0.065	0.038	0.053	0.064	0.092	0.020	0.022	0.020	0.021	0.045	0.043	<u>0.044</u>	0.054	0.063	0.067	0.070	0.082	0.055	0.060	0.065	0.072
FEDformer	RMSE	0.088	0.092	0.101	0.109	0.067	0.082	0.105	0.183	0.036	0.042	0.042	0.042	0.072	0.072	0.075	<u>0.077</u>	0.096	0.100	0.105	0.116	0.087	0.093	0.102	0.108
	MAE	0.050	0.051	0.057	0.064	0.050	0.064	0.080	0.151	0.022	0.023	0.022	0.022	0.049	0.049	0.051	0.055	0.072	0.076	0.080	0.090	0.063	0.068	0.075	0.081
Autoformer	RMSE	0.104	0.103	0.101	0.110	0.066	0.083	0.101	0.181	0.042	0.050	0.053	0.050	0.075	0.099	0.115	0.119	0.105	0.114	0.119	0.136	0.109	0.112	0.125	0.126
	MAE	0.064	0.061	0.059	0.065	0.050	0.063	0.075	0.150	0.026	0.033	0.034	0.035	0.051	0.051	0.051	0.088	0.116	0.079	0.086	0.088	0.102	0.081	0.083	0.091
Informer	RMSE	0.139	0.134	0.115	0.132	0.084	0.088	0.127	0.170	0.039	0.047	0.053	0.054	0.124	0.138	0.144	0.148	0.121	0.137	0.145	0.157	0.096	0.107	0.119	0.149
	MAE	0.101	0.097	0.101	0.132	0.066	0.068	0.093	0.117	0.023	0.030	0.034	0.035	0.094	0.105	0.112	0.116	0.093	0.103	0.112	0.125	0.070	0.082	0.090	0.115
Reformer	RMSE	0.152	0.201	0.203	0.228	0.146	0.169	0.189	0.201	0.053	0.054	0.053	0.054	0.125	0.138	0.144	0.148	0.143	0.148	0.155	0.089	0.108	0.128	0.163	
	MAE	0.108	0.147	0.154	0.173	0.126	0.147	0.157	0.166	0.035	0.035	0.035	0.035	0.095	0.121	0.122	0.120	0.113	0.120	0.124	0.126	0.065	0.081	0.100	0.132

The WM-MLP backbone results reported in Table 1 consider an optimization with respect

to p , the number of windows, while the HC-MLP considers a fixed size of $p = 4$ windows. Thus, for a more suitable comparison, Table 2 shows a comparison of the FIA-Net performance under both backbones with $p = 4$. We note that when p is similar for both models, the FIA-Net attains similar results under both backbones, while the HC-MLP requires significantly fewer parameters. Consequently, when the number of windows allows for an HC-MLP version (e.g., $p = 2^\ell$ as we further explain in Appendix C), an HC-MLP backbone is preferable.

Table 2: Performance comparison between WM-MLP and HC-MLP with a fixed number of STFT windows ($p = 4$). Results demonstrate that HC-MLP achieves comparable accuracy while significantly reducing model parameters, making it preferable for efficient implementations.

	Metric	Traffic				ETTh1				ETTm1			
		96	192	336	720	96	192	336	720	96	192	336	720
WM-MLP ($p = 4$)	RMSE	0.033	0.034	0.035	0.036	0.088	0.094	0.100	0.103	0.074	0.082	0.089	0.096
	MAE	0.016	0.016	0.017	0.018	0.058	0.064	0.068	0.075	0.049	0.056	0.060	0.067
HC-MLP	RMSE	0.032	0.034	0.035	0.036	0.083	0.085	0.094	0.101	0.072	0.082	0.089	0.096
	MAE	0.016	0.017	0.017	0.018	0.049	0.057	0.064	0.068	0.049	0.056	0.060	0.067

5.3 Ablation Studies

We consider three ablation studies that best demonstrate the key aspects of the proposed work. We focus on the effect of frequency selection, the size of the lookback window, and the omission of real/imaginary components in the training procedure. We show that, in various cases, the total amount of parameters can be decreased by up to 60%. Due to space limitations, the results are demonstrated on a single dataset, while a full discussion and additional results are given in Appendix D.4.

5.3.1 Frequency Dimension Compression

We study the effect of the parameter M in the top- M frequency component selection process on the ETTh dataset. As seen in figure 5, even though the model performance varies over different datasets and forecasting horizon sizes, in most cases, $M = 4$ attains the best accuracy. Furthermore, note that taking $M < M_{\max} = \frac{N_{FFT}}{2} + 1$ improves the model’s results. We conjecture that considering fewer frequency components decreases the NN class complexity, which potentially simplifies the optimization procedure landscape while preserving most of the information contained within the signal. We expand upon this discussion and provide additional results in the Appendix D.1.

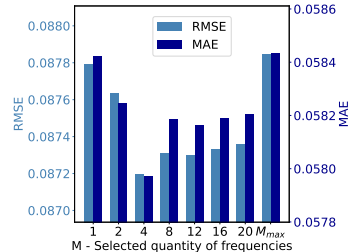


Figure 5: Accuracy vs. M

5.3.2 Effect of Lookback Window Size

In this section, we evaluate the impact of varying lookback window sizes $L \in \{24, 48, 96, 192, 288, 480, 576, 720\}$ for different prediction lengths $T \in \{96, 192, 336, 720\}$. As shown in Figure 6, the dotted line represents the RMSE, while the solid line represents the MAE. The model’s performance initially improves as L increases, as expected, since a longer lookback provides more contextual information. However, many models exhibit parabolic behavior, where performance deteriorates after a certain point due to overfitting to noise or unrealistic patterns in the data. In contrast, our model maintains stable performance and effectively avoids overfitting, demonstrating its robustness to changes in lookback window size. Additional experiments can be found in Appendix D.2.

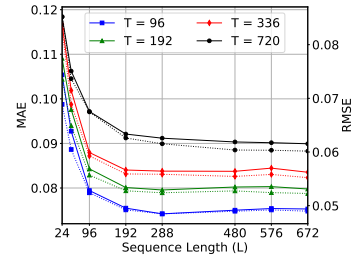


Figure 6: Accuracy vs. L .

5.3.3 Redundancy of Complex Representation

We study the effect of the real and imaginary components on prediction quality. We fix the hyperparameters $E = 128$, $p = 13$, $N_{FFT} = 16$, $M = M_{\max}$, and compare several scenarios, such that each scenario considers the masking of a different component, either in the data, the parameters, or both. The masking occurs in both training and inference. As seen in Table 3, the elimination of either the real or imaginary components in the data does not significantly affect the downstream accuracy, which may hint at redundancy in the learning procedure. Furthermore, this redundancy is maintained when we consider the intersection omission of the real/imaginary parts of both the data and the MLP weights. This phenomenon can be explained through the Kramers-Kronig relation (KKR) [42, 43], which provides a representation of the real component of an analytic complex-valued function in terms of its complex components and vice versa. Roughly speaking, for a complex-valued function $c(\omega) = \text{Re}\{c\}(\omega) + i\text{Im}\{c\}(\omega)$, the KKR are given by

$$\text{Re}\{c\}(\omega) = \frac{1}{\pi} \int_{-\infty}^{\infty} \frac{\text{Im}\{c\}(\sigma)}{\omega - \sigma} d\sigma, \quad \text{Im}\{c\}(\omega) = -\frac{1}{\pi} \int_{-\infty}^{\infty} \frac{\text{Re}\{c\}(\sigma)}{\omega - \sigma} d\sigma.$$

Thus, we conjecture that masking one component forces the other to recover both in the learning procedure by implicitly approximating the KRR. We therefore believe that a sophisticated system design that considers a KRR-based architecture may lead to the sufficiency of a single component in the forecasting task but leaves a complete study of that subject to future work. This phenomenon is further explored in Appendix 8.

6 Conclusion

This paper presents FIA-Net, a new model for long-term time series forecasting using STFT window aggregation in the frequency domain and HC MLPs. The proposed methodology shows superior performance over existing SoTA on standard benchmark datasets. We show that treating the set of STFT windows as a single HC tensor, which is processed by a novel HC-MLP, significantly reduces the total amount of parameters, with no degradation in the TSF accuracy. We study various schemes to increase model efficiency by, for example, choosing the top- M magnitude frequency components. Experimental results show that the omission

Dataset	I/O	96/96		96/192		96/336		96/720	
	Hidden Part	MAE	RMSE	MAE	RMSE	MAE	RMSE	MAE	RMSE
ETTM1	X^{Real}	0.0522	0.0797	0.0560	0.0850	0.0597	0.0888	0.0658	0.0958
	X^{Imag}	0.0521	0.0792	0.0562	0.0844	0.0592	0.0879	0.0684	0.0976
	W^{Real}	0.0522	0.0791	0.0557	0.0843	0.0588	0.0875	0.0669	0.0964
	W^{Imag}	0.0526	0.0801	0.0560	0.0849	0.0596	0.0888	0.0651	0.0953
	$W^{\text{Imag}}, X^{\text{Imag}}$	0.0523	0.0798	0.0560	0.0849	0.0592	0.0884	0.0644	0.0947
	$W^{\text{Real}}, X^{\text{Real}}$	0.0522	0.0791	0.0557	0.0843	0.0588	0.0887	0.0669	0.0930
	\emptyset	0.0522	0.0791	0.0565	0.0848	0.0592	0.0878	0.0685	0.0975

Table 3: Performance comparison on ETTm1 for $I/O = 96 \times \{96, 192, 336, 720\}$ with various modes. $X^{\text{Real}}/X^{\text{Imag}}$ hide the real/imaginary parts of the input, while $W^{\text{Real}}/W^{\text{Imag}}$ zero out the corresponding weights. Completely ignoring both components is denoted as $(W^{\text{Imag}}, X^{\text{Imag}})$ or $(W^{\text{Real}}, X^{\text{Real}})$.

of one of the complex representation components does not induce notable segregation in performance, which may be explained by the KKR. For future work, we aim to leverage the KKR equations to propose a forecasting model that only considers the real component in the complex representation while operating over the complex plane. Additionally, we plan to further investigate the relationship between the number of adjacent STFT windows in the WM-MLP backbone and the statistical properties of the datasets.

References

- [1] R. A. Rajagukguk, R. A. Ramadhan, and H.-J. Lee. A review on deep learning models for forecasting time series data of solar irradiance and photovoltaic power. *Energies*, 13(24):6623, 2020.
- [2] X. Chen and R. Chen. A review on traffic prediction methods for intelligent transportation system in smart cities. In *2019 12th International Congress on Image and Signal Processing, BioMedical Engineering and Informatics (CISP-BMEI)*, pages 1–5. IEEE, 2019.
- [3] O. B. Sezer, M. U. Gudelek, and A. M. Ozbayoglu. Financial time series forecasting with deep learning: A systematic literature review: 2005–2019. *Applied Soft Computing*, 90:106181, 2020.
- [4] J. Zhang and K.-F. Man. Time series prediction using rnn in multi-dimension embedding phase space. In *Proceedings of the IEEE International Conference on Systems, Man, and Cybernetics (SMC)*, pages 1868–1873. IEEE, 1998.
- [5] A. Graves. Supervised sequence labelling with recurrent neural networks. *Studies in Computational Intelligence*, 385:37–45, 2012.
- [6] J. Chung, C. Gulcehre, K. Cho, and Y. Bengio. Empirical evaluation of gated recurrent neural networks on sequence modeling. *arXiv preprint arXiv:1412.3555*, 2014.

- [7] A. Vaswani, S. Bengio, E. Brevdo, F. Chollet, A. N. Gomez, S. Gouws, L. Jones, Ł. Kaiser, N. Kalchbrenner, N. Parmar, R. Sepassi, N. Shazeer, and J. Uszkoreit. Tensor2tensor for neural machine translation. CoRR, abs/1803.07416, 2018.
- [8] T. Zhou, Z. Ma, Q. Wen, X. Wang, L. Sun, and R. Jin. FEDformer: Frequency enhanced decomposed transformer for long-term series forecasting. In Proc. 39th International Conference on Machine Learning (ICML 2022), 2022.
- [9] H. Wu, J. Xu, J. Wang, and M. Long. Autoformer: Decomposition transformers with Auto-Correlation for long-term series forecasting. In Advances in Neural Information Processing Systems (NeurIPS), 2021.
- [10] Y. Zhang and J. Yan. Crossformer: Transformer utilizing cross-dimension dependency for multivariate time series forecasting. In The Eleventh International Conference on Learning Representations (ICLR), 2023.
- [11] R. Pascanu, T. Mikolov, and Y. Bengio. On the difficulty of training recurrent neural networks. arXiv preprint arXiv:1211.5063v2, 2013. Available at: <https://arxiv.org/abs/1211.5063>.
- [12] D. Kim, J. Park, J. Lee, and H. Kim. Are self-attentions effective for time series forecasting? arXiv preprint arXiv:2405.16877, 2024.
- [13] Z. Wu, S. Pan, G. Long, J. Jiang, X. Chang, and C. Zhang. Connecting the dots: Multivariate time series forecasting with graph neural networks. In Proceedings of the 26th ACM SIGKDD International Conference on Knowledge Discovery & Data Mining (KDD), pages 753–763, 2020.
- [14] B. N. Oreshkin, D. Carпов, N. Chapados, and Y. Bengio. N-beats: Neural basis expansion analysis for interpretable time series forecasting. arXiv preprint arXiv:1905.10437, 2019.
- [15] K. Yi, Q. Zhang, L. Cao, S. Wang, G. Long, L. Hu, H. He, Z. Niu, W. Fan, and H. Xiong. A survey on deep learning based time series analysis with frequency transformation. Journal of the ACM, 37(4):111, 2023.
- [16] K. Yi, Q. Zhang, W. Fan, S. Wang, P. Wang, H. He, N. An, D. Lian, L. Cao, and Z. Niu. Frequency-domain MLPs are more effective learners in time series forecasting. In Thirty-seventh Conference on Neural Information Processing Systems (NeurIPS), 2023.
- [17] R. Shen, L. Liu, B. Wang, Y. Guan, Y. Yang, and J. Jiang. Freqtsf: Time series forecasting via simulating frequency kramer-kronig relations. arXiv preprint arXiv:2407.21275, 2024.
- [18] D. Gabor. Theory of communication. part 1: The analysis of information. Journal of the Institution of Electrical Engineers-Part III: Radio and Communication Engineering, 93(26):429–441, 1946.
- [19] G. E. P. Box and G. M. Jenkins. Some recent advances in forecasting and control. Journal of the Royal Statistical Society: Series C (Applied Statistics), 17(2):91–109, 1968.

- [20] G. E. P. Box and D. A. Pierce. Distribution of residual autocorrelations in autoregressive-integrated moving average time series models. Journal of the American Statistical Association, 65:1509–1526, 1970.
- [21] M. W. Watson. Vector autoregressions and cointegration. Technical report, Princeton University, 1993.
- [22] H. Zhou, J. Li, S. Zhang, S. Zhang, M. Yan, and H. Xiong. Expanding the prediction capacity in long sequence time-series forecasting. Artificial Intelligence, 318:103886, 2023.
- [23] N. Kitaev, Ł. Kaiser, and A. Levskaya. Reformer: The efficient transformer. In International Conference on Learning Representations (ICLR), 2020. arXiv preprint arXiv:2001.04451.
- [24] Y. Nie, N. H. Nguyen, P. Sinthong, and J. Kalagnanam. A time series is worth 64 words: Long-term forecasting with transformers. In International Conference on Learning Representations (ICLR), 2023.
- [25] L. Bai, L. Yao, C. Li, X. Wang, and C. Wang. Adaptive graph convolutional recurrent network for traffic forecasting. In Advances in Neural Information Processing Systems (NeurIPS), 2020.
- [26] S. Woo, S. Lee, J. Kim, S. Kim, H. Kim, and W. Jang. Etsformer: Exponential smoothing transformer for time-series forecasting. In Proceedings of the 38th International Conference on Machine Learning (ICML), 2022.
- [27] T. Zhou, Z. Ma, Q. Wen, X. Wang, L. Sun, T. Yao, W. Yin, and R. Jin. Film: Frequency improved legendre memory model for long-term time series forecasting. arXiv preprint arXiv:2205.08897, 2022.
- [28] L. Zhang, C. C. Aggarwal, and G.-J. Qi. Stock price prediction via discovering multi-frequency trading patterns. In Proceedings of the 23rd ACM SIGKDD International Conference on Knowledge Discovery and Data Mining (KDD), pages 2141–2149, 2017.
- [29] L. Cao, K. Yi, L. Hu, Q. Zhang, N. Cao, and Z. Niu. Stemgnn: Graph neural networks for multivariate time series forecasting. In Proceedings of the 37th International Conference on Machine Learning (ICML), 2020.
- [30] W. R. Hamilton. On quaternions; or on a new system of imaginaries in algebra. Proceedings of the Royal Irish Academy, 1844.
- [31] T. Parcollet, M. Morchid, P.-M. Bousquet, R. Dufour, and G. Linares. Quaternion convolutional neural networks for image classification and compression. In Proceedings of the IEEE Spoken Language Technology Workshop (SLT), pages 362–368. IEEE, 2016.
- [32] L. Luo, H. Feng, and L. Ding. Color image compression based on quaternion neural network principal component analysis. In 2010 International Conference on Multimedia Technology, pages 1–4. IEEE, 2010.
- [33] L. S. Saoud and H. Al-Marzouqi. Metacognitive sedenion-valued neural network and its learning algorithm. IEEE Access, 8:144823–144836, 2020.

- [34] R. Kycia and A. Niemczynowicz. Hypercomplex neural network in time series forecasting of stock data. arXiv preprint arXiv:2401.04632, 2024.
- [35] K. Yi, Q. Zhang, L. Hu, N. Cao, and Z. Niu. Cost: A contrastive framework for self-supervised time series representation learning. In Advances in Neural Information Processing Systems (NeurIPS), 2022.
- [36] S. B. Davis and P. Mermelstein. Comparison of parametric representations for monosyllabic word recognition in continuously spoken sentences. IEEE Transactions on Acoustics, Speech, and Signal Processing, 28(4):357–366, 1980.
- [37] P. Fryzlewicz and H. Cho. Multiple-change-point detection for auto-regressive conditional heteroscedastic processes. Journal of the Royal Statistical Society: Series B (Statistical Methodology), 76(5):903–924, 2014.
- [38] K. V. Khmelnitskaya and M. Shapiro. Function theories in cayley-dickson algebras and number theory. Complex Analysis and Operator Theory, 15(2):1–40, 2021.
- [39] Ailing Zeng, Muxi Chen, Lei Zhang, and Qiang Xu. Are transformers effective for time series forecasting? In Proceedings of the AAAI Conference on Artificial Intelligence, 2023.
- [40] A. Paszke, S. Gross, F. Massa, A. Lerer, J. Bradbury, G. Chanan, T. Killeen, Z. Lin, N. Gimelshein, L. Antiga, et al. Pytorch: An imperative style, high-performance deep learning library. Advances in Neural Information Processing Systems (NeurIPS), 32, 2019.
- [41] D. P. Kingma. Adam: A method for stochastic optimization. arXiv preprint arXiv:1412.6980, 2014.
- [42] R. de L. Kronig. On the theory of dispersion of x-rays. Journal of the Optical Society of America, 12(6):547–557, 1926.
- [43] H. A. Kramers. La diffusion de la lumière par les atomes. In Atti del Congresso Internazionale dei Fisici, Como, volume 2, pages 545–557, 1927.
- [44] I. L. Kantor and A. S. Solodovnikov. Hypercomplex Numbers: An Elementary Introduction to Algebras. Springer-Verlag, 1989.

Appendix

A Notations & Symbols

A.1 Notation

We provide a detailed table of the involved notation in this paper:

Symbol	Description
B	Batch size.
L	Lookback window size.
D	Number of features for each time step.
T	Length of the prediction horizon.
E	Embedding size.
M	Number of frequencies to select from all the frequencies using the top M magnitudes.
X	Multivariate time series with a lookback window of size L at timestamps t .
X_t	Multivariate values of D distinct series at timestamp t .
$X_{t,i}$	The value of the i -th feature of the distinct series at timestamp t .
\hat{X}	Ground truth target values.
σ	activation function
P	Number of windows in the STFT.
N_{FFT}	Number of frequency bins in each window of the STFT.
ω	Window function for the STFT.
X_E	X after traversing through the embedding layer.
X_{Rec}	The reconstructed X after the frequency alteration.
c_i^t	The i -th window of the input in the time domain.
C_i	The i -th window of the STFT containing N_{FFT} frequency bins.
C_i^{in}	The i -th window of the STFT, retaining the top M frequency components based on magnitude.
C_i^{out}	The i -th window of the STFT after the WM-MLP/WHC has been applied.
$W_{i \rightarrow j}$	The weights that capture the frequency energy shift between window i and j , defined as $W_{i \rightarrow j} = W_{i \rightarrow j}^{\text{Real}} + jW_{i \rightarrow j}^{\text{Img}}$, where $W_{i \rightarrow j} \in \mathbb{C}^{E \times E}$.
$B_{i \rightarrow j}$	The bias that capture the frequency energy shift between windows i and j , defined as $B_{i \rightarrow j} = B_{i \rightarrow j}^{\text{Real}} + jB_{i \rightarrow j}^{\text{Img}}$, where $B_{i \rightarrow j} \in \mathbb{C}^E$.

Table 4: Table of Symbols and Descriptions

A.2 Dimensions

The following table summarizes the dimensions of the data tensor in every step of the FIA-Net.

Symbol	Dimension
X	$\mathbb{R}^{B \times L \times D}$
X_E	$\mathbb{R}^{B \times L \times D \times E}$
C_i	$\mathbb{C}^{B \times N_{FFT} \times D \times E}$
C_i^M	$\mathbb{C}^{B \times M \times D \times E}$
$C_i^{\text{in/out}}$	$\mathbb{C}^{B \times M \times D \times E}$
X_{Rec}	$\mathbb{R}^{B \times L \times D \times E}$
\hat{X}	$\mathbb{R}^{B \times T \times D}$

Table 5: Table of Symbols and Dimension

B Additional Experimental Details

B.1 Dataset Descriptions

In our experiments, we utilized thirteen real-world datasets to assess the effectiveness of models for long-term TSF. Below, we provide the details of these datasets, categorized by their forecasting horizon.

- **Exchange:** This dataset includes daily exchange rates for eight countries (Australia, Britain, Canada, Switzerland, China, Japan, New Zealand, and Singapore) from 1990 to 2016.
- **Weather:** This dataset gathers 21 meteorological indicators, including humidity and air temperature, from the Weather Station of the Max Planck Biogeochemistry Institute in Germany in 2020. The data is collected every 10 minutes.
- **Traffic:** For long-term forecasting, this dataset includes hourly traffic data from 862 freeway lanes in San Francisco, with data collected since January 1, 2015.
- **Electricity:** For long-term forecasting, this dataset covers electricity consumption data from 321 clients, with records starting from January 1, 2011, and a sampling interval of 15 minutes.
- **ETT:** This dataset is sourced from two electric transformers, labeled ETTh1 and ETTm1, with two different resolutions: 15 minutes and 1 hour. These are used as benchmarks for long-term forecasting.

Datasets	Weather	Traffic	Electricity	ETTh1	ETTm1	Exchange Rates
Features	21	862	321	7	7	8
Timesteps	52696	17544	26304	17420	69680	7588
Frequency	10m	1h	1h	1h	15m	1d
Lookback Window	96	48	96	96	96	96
Prediction Length	96, 192, 336, 720	96, 192, 336, 720	96, 192, 336, 720	96, 192, 336, 720	96, 192, 336, 720	96, 192, 336, 720

Table 6: Long Term Datasets Parameters

B.2 baselines

We employ a selection of SoTA representative models for our comparative analysis, focusing on Transformer-based architectures and other popular models. The models included are as follows:

- **Informer**: Informer enhances the efficiency of self-attention mechanisms to effectively capture dependencies across variables. The source code was obtained from [GitHub](#), and we utilized the default configuration with a dropout rate of 0.05, two encoder layers, one decoder layer, a learning rate of 0.0001, and the Adam optimizer.
- **Reformer**: Reformer combines the power of Transformers with efficient memory and computation management, especially for long sequences. The source code was sourced from [GitHub](#), and we employed the recommended configuration for our experiments.
- **Autoformer**: Autoformer introduces a decomposition block embedded within the model to progressively aggregate long-term trends from intermediate predictions. The source code was accessed from [GitHub](#), and we followed the recommended settings for all experiments.
- **FEDformer**: FEDformer introduces an attention mechanism based on low-rank approximation in the frequency domain combined with a mixture of expert decomposition to handle distribution shifts. The source code was retrieved from [GitHub](#). We utilized the Frequency Enhanced Block (FEB-f) and selected the random mode with 64 as the experimental configuration.
- **LTSF-Linear**: LTSF-Linear is a minimalist model employing simple one-layer linear models to learn temporal relationships in time series data. We used it as our baseline for long-term forecasting, downloading the source code from [GitHub](#), and adhered to the default experimental settings.
- **PatchTST**: PatchTST is a Transformer-based model designed for TSF, introducing patching and a channel-independent structure to enhance model performance. The source code was obtained from [GitHub](#), and we used the recommended settings for all experiments.
- **FreTS**: FRETS is a sophisticated model tailored for efficient TSF by exploiting a frequency domain approach. The implementation is available on [GitHub](#), and we utilized

the default configuration as recommended by the authors. In our work, FRETS serves as the foundational model. We address its limitations, particularly its handling of non-stationary data, while adapting its strengths, such as its complex frequency learner. To fully grasp the contributions of this paper, we recommend reviewing FRETS in detail first.

B.3 Implementation Details

Table 7 lists the hyperparameter values used in the FIA-Net implementation. Both WM-MLP and HC-MLP backbones are implemented with the same hyperparameter values, except for p , the number of STFT windows.

DataSets	Weather	Traffic	Electricity	ETTh1	ETTm1	Exchange rate
Batch Size	16	4	4	8	8	8
Embed Size	128	32	64	128	128	128
Hidden Size	256	256	256	256	256	256
NFF	16	32	32	6	48	32
STFT Windows	7	13	13	33	4	13
S-M	10	M_{\max}	4	4	4	M_{\max}
Epoch	10	10	10	10	10	10

Table 7: Hyperparameter Settings for Long-Term Datasets for the WM-MLP and HC-MLP

B.4 Evaluation Metrics

In this study, we use the Mean Squared Error (MSE) as the loss function during training. However, for evaluation, we report both the Mean Absolute Error (MAE) and the Root Mean Squared Error (RMSE).

which are defined as follows:

$$\text{MSE} = \frac{1}{n} \sum_{i=1}^n (Y_i - \hat{Y}_i)^2, \quad \text{RMSE} = \sqrt{\frac{1}{n} \sum_{i=1}^n (Y_i - \hat{Y}_i)^2}, \quad \text{MAE} = \frac{1}{n} \sum_{i=1}^n |Y_i - \hat{Y}_i|$$

Where:

- Y_i represents the true target values,
- \hat{Y}_i represents the predicted values,
- n is the total number of samples.

B.5 Normalization Methods

In this study, similar to the FRETS model [16], we apply min-max normalization to standardize the input data to the range between 0 and 1. This method helps in ensuring that all features contribute equally to the model and prevents any specific feature from dominating due to differences in scale. The formula for min-max normalization is given by:

$$X_{Norm} = \frac{X - X_{\min}}{X_{\max} - X_{\min}}$$

By normalizing the data, we ensure that all input features are within the same range, which can improve model convergence and performance.

C Additional Information on HC Numbers and Models

In this section we extend the discussion on HC numbers, considering additional values of p beyond $p = 4$. We couple the presentation with the construction of the corresponding HC-MLP in the considered base. Recall that the base of a HC number, i.e., the number of its components is given by $b = 2p$. While hyper-complex number can be defined for any value of b , most research has been performed on b that is given by a power of 2, as the resulting structure of the (algebraic) field. The addition of two HC numbers is simply given by the component-wise summation. In what follows, we focus on HC multiplication and additional properties. For more information on the HC number system, we refer the reader to [44].

C.1 Base 2 - Complex Numbers

When $b = 2$, the resulting field is the complex plane \mathbb{C} . We describe \mathbb{C} for completeness of presentation. Given two complex numbers $C_1 = \alpha_1 + j\alpha_2$ and $C_2 = \beta_1 + j\beta_2$, where $\alpha_1, \alpha_2, \beta_1, \beta_2$ are real numbers, their complex multiplication is defined as:

$$C_1 \cdot C_2 = (\alpha_1\beta_1 - \alpha_2\beta_2) + j(\alpha_1\beta_2 + \alpha_2\beta_1)$$

The norm of a complex number is given by:

$$|C_1|_{\mathbb{C}} = \sqrt{\alpha_1^2 + \alpha_2^2},$$

which is preserved under multiplication, i.e.,

$$|C_1 \cdot C_2|_{\mathbb{C}} = |C_1|_{\mathbb{C}} \cdot |C_2|_{\mathbb{C}}.$$

Since the STFT with a single window ($p = 1$) is equivalent to the standard FFT, applying our method for hyper-complex number MLP results in the following equation:

$$C_{\text{in}} = \text{FFT}(X)$$

$$C^{\text{out}} = \sigma(C_{\text{Real}}^{\text{in}} \cdot W_{1,\text{Real}} - C_{\text{Imag}}^{\text{in}} \cdot W_{1,\text{Imag}} + B_{1,\text{Real}}) + \sigma(j(C_{\text{Real}}^{\text{in}} \cdot W_{1,\text{Imag}} + C_{\text{Imag}}^{\text{in}} \cdot W_{1,\text{Real}} + B_{1,\text{Imag}}))$$

Here, $W_i \in \mathbb{C}^{E \times E}$ denotes the layer weights, $B \in \mathbb{C}^E$ represents the bias term, and the multiplication occurs across the embedding dimension. Note that for $b = 2$ the HV formulation boils down to the one from [16]. Thus, the HC-MLP can be considered as an HC generalization of the FD-MLP. which allows for efficient window aggregation.

C.2 Base 4 - Quaternions

Denote the field of Quaternions with $\tilde{\mathbb{Q}}$. We represent Quaternions with a couple of Complex number, i.e., for $H_1, H_2 \in \tilde{\mathbb{Q}}$, $H_1 = (\alpha_1, \alpha_2)$ and $H_2 = (\beta_1, \beta_2)$, their multiplication is defined as

$$H_1 \cdot H_2 = (\alpha_1\beta_1 - \overline{\alpha_2}\beta_2, \quad \alpha_2\overline{\beta_1} + \alpha_1\beta_2)$$

The norm of a quaternion is given by:

$$|q|_{\tilde{\mathbb{Q}}} = \sqrt{|\alpha_1|_{\mathbb{C}}^2 + |\alpha_2|_{\mathbb{C}}^2}$$

The norm is preserved under multiplication, meaning:

$$|q_1 \cdot q_2|_{\tilde{\mathbb{Q}}} = |q_1|_{\tilde{\mathbb{Q}}} \cdot |q_2|_{\tilde{\mathbb{Q}}}$$

For our model, the corresponding HC-MLP (which we denote QuatMLP) operating on $C^{\text{in}} = (C_1^{\text{in}}, C_2^{\text{in}}) \in \tilde{\mathbb{Q}}$, is given by,

$$C^{\text{out}} = \text{QuatMLP}(C^{\text{in}}) = \sigma(C^{\text{in}} \cdot W + B)$$

where:

$$C_1^{\text{out}} = \sigma(C_1 \cdot W_1 - \overline{C_2} \cdot W_2 + B_1), \quad C_2^{\text{out}} = \sigma(C_2 \cdot \overline{W_1} + C_1 \cdot W_2 + B_2).$$

Here, $W_i \in \mathbb{C}^{E \times E}$, $i = 1, 2$ denote the layer weights, $B \in \mathbb{C}^E$ represents the bias term, and the multiplication involves complex MLP operations across the embedding dimension.

C.3 Base 16 - Sedenions

Elements on the Sedenions field, denoted \mathbb{S} , are denoted with 8-tuples of complex numbers. Given two sedenions represented by complex numbers $S_1, S_2 \in \mathbb{S}$, $S_1 = (\alpha_1, \alpha_2, \dots, \alpha_8)$ and $S_2 = (\beta_1, \beta_2, \dots, \beta_8)$, their multiplication is given by

$$S_1 \cdot S_2 = \begin{pmatrix} \alpha_1\beta_1 - \alpha_2\overline{\beta_2} - \alpha_3\overline{\beta_3} - \alpha_4\overline{\beta_4} - \alpha_5\overline{\beta_5} - \alpha_6\overline{\beta_6} - \alpha_7\overline{\beta_7} - \alpha_8\overline{\beta_8} \\ \alpha_1\beta_2 + \alpha_2\beta_1 + \alpha_3\overline{\beta_4} - \alpha_4\overline{\beta_3} + \alpha_5\overline{\beta_6} - \alpha_6\overline{\beta_5} + \alpha_7\overline{\beta_8} - \alpha_8\overline{\beta_7} \\ \alpha_1\beta_3 - \alpha_2\overline{\beta_4} + \alpha_3\beta_1 + \alpha_4\beta_2 + \alpha_5\overline{\beta_7} - \alpha_6\overline{\beta_8} - \alpha_7\overline{\beta_5} + \alpha_8\overline{\beta_6} \\ \alpha_1\beta_4 + \alpha_2\beta_3 - \alpha_3\overline{\beta_2} + \alpha_4\beta_1 + \alpha_5\overline{\beta_8} + \alpha_6\overline{\beta_7} - \alpha_7\overline{\beta_6} - \alpha_8\overline{\beta_5} \\ \alpha_1\beta_5 - \alpha_2\overline{\beta_6} - \alpha_3\overline{\beta_7} - \alpha_4\overline{\beta_8} + \alpha_5\beta_1 + \alpha_6\beta_2 + \alpha_7\beta_3 + \alpha_8\beta_4 \\ \alpha_1\beta_6 + \alpha_2\beta_5 - \alpha_3\overline{\beta_8} + \alpha_4\overline{\beta_7} - \alpha_5\beta_2 + \alpha_6\beta_1 - \alpha_7\beta_4 + \alpha_8\beta_3 \\ \alpha_1\beta_7 + \alpha_2\beta_8 + \alpha_3\beta_5 - \alpha_4\beta_6 - \alpha_5\beta_3 + \alpha_6\beta_4 + \alpha_7\beta_1 - \alpha_8\beta_2 \\ \alpha_1\beta_8 - \alpha_2\beta_7 + \alpha_3\beta_6 + \alpha_4\beta_5 - \alpha_5\beta_4 - \alpha_6\beta_3 + \alpha_7\beta_2 + \alpha_8\beta_1 \end{pmatrix}$$

where each component follows the rules of Complex multiplication. The norm of a sedenion is given by:

$$|S|_{\mathbb{S}} = \sqrt{\sum_{j=1}^8 |\alpha_j|_{\mathbb{C}}^2}$$

Unlike nase 2, 4 and 8, Sedenions *do not* preserve the norm under addition and multiplication.

The base-16 HC-MLP, denoted SedMLP, operating on an input C^{in} from the STFT with multiple windows $C^{\text{in}} = (C_j^{\text{in}})_{j=1}^8$, is given by

$$C^{\text{out}} = \text{SedMLP}(C^{\text{in}}) = \sigma(C^{\text{in}} \cdot W + B)$$

where:

$$\begin{aligned}
C_1^{\text{out}} &= \sigma (C_1^{\text{in}}W_1 - C_2^{\text{in}}\overline{W_2} - C_3^{\text{in}}\overline{W_3} - C_4^{\text{in}}\overline{W_4} - C_5^{\text{in}}\overline{W_5} - C_6^{\text{in}}\overline{W_6} - C_7^{\text{in}}\overline{W_7} - C_8^{\text{in}}\overline{W_8} + B_1) \\
C_2^{\text{out}} &= \sigma (C_1^{\text{in}}W_2 + C_2^{\text{in}}W_1 + C_3^{\text{in}}\overline{W_4} - C_4^{\text{in}}\overline{W_3} + C_5^{\text{in}}\overline{W_6} - C_6^{\text{in}}\overline{W_5} + C_7^{\text{in}}\overline{W_8} - C_8^{\text{in}}\overline{W_7} + B_2) \\
C_3^{\text{out}} &= \sigma (C_1^{\text{in}}W_3 - C_2^{\text{in}}\overline{W_4} + C_3^{\text{in}}W_1 + C_4^{\text{in}}W_2 + C_5^{\text{in}}\overline{W_7} - C_6^{\text{in}}\overline{W_8} - C_7^{\text{in}}\overline{W_5} + C_8^{\text{in}}\overline{W_6} + B_3) \\
C_4^{\text{out}} &= \sigma (C_1^{\text{in}}W_4 + C_2^{\text{in}}W_3 - C_3^{\text{in}}W_2 + C_4^{\text{in}}W_1 + C_5^{\text{in}}\overline{W_8} + C_6^{\text{in}}\overline{W_7} - C_7^{\text{in}}\overline{W_6} - C_8^{\text{in}}\overline{W_5} + B_4) \\
C_5^{\text{out}} &= \sigma (C_1^{\text{in}}W_5 - C_2^{\text{in}}\overline{W_6} - C_3^{\text{in}}\overline{W_7} - C_4^{\text{in}}\overline{W_8} + C_5^{\text{in}}W_1 + C_6^{\text{in}}W_2 + C_7^{\text{in}}W_3 + C_8^{\text{in}}W_4 + B_5) \\
C_6^{\text{out}} &= \sigma (C_1^{\text{in}}W_6 + C_2^{\text{in}}W_5 - C_3^{\text{in}}\overline{W_8} + C_4^{\text{in}}\overline{W_7} - C_5^{\text{in}}W_2 + C_6^{\text{in}}W_1 - C_7^{\text{in}}W_4 + C_8^{\text{in}}W_3 + B_6) \\
C_7^{\text{out}} &= \sigma (C_1^{\text{in}}W_7 + C_2^{\text{in}}W_8 + C_3^{\text{in}}W_5 - C_4^{\text{in}}W_6 - C_5^{\text{in}}W_3 + C_6^{\text{in}}W_4 + C_7^{\text{in}}W_1 - C_8^{\text{in}}W_2 + B_7) \\
C_8^{\text{out}} &= \sigma (C_1^{\text{in}}W_8 - C_2^{\text{in}}W_7 + C_3^{\text{in}}W_6 + C_4^{\text{in}}W_5 - C_5^{\text{in}}W_4 - C_6^{\text{in}}W_3 + C_7^{\text{in}}W_2 + C_8^{\text{in}}W_1 + B_8)
\end{aligned}$$

Here, $W_i \in \mathbb{C}^{E \times E}$, $i = 1, \dots, 8$ denotes the layer weights, $B \in \mathbb{C}^E$ represents the bias term, and the multiplication involves complex MLP operations across the embedding dimension.

D Additional Ablation Studies

This section presents additional ablation studies, expanding on the findings reported in Section 5.3. We analyze the impact of FFT resolution, embedding size, and the number of STFT windows on WM-MLP performance. Additionally, we include further results for the frequency compression, sequence length, and real vs. imaginary component discussions. Furthermore, we provide a comparative analysis of various hyper-complex fields (octonions, quaternions, and sedenions) for the HC-MLP and report the corresponding results.

D.1 Parameter Sensitivity

In this section, we conduct a parameter sweep to examine the effects of different hyperparameters on model performance. To accomplish this, we utilize two datasets: the ETTh1 dataset and the electricity dataset. Each section presents four graphs illustrating the results on the two datasets for a configuration of $I/O = 96 \times 96, 336$. Except for the specific experiment sweep, the embedding size is set to 128 for the ETTh1 dataset and 64 for the electricity dataset, with M set to 0 for all datasets.

Embed Size In this section, we evaluate the influence of embedding size on the model’s performance. We conducted experiments with embedding dimensions $E \in \{1, 2, 4, 8, 16, 32, 64, 128, 256, 512\}$, while keeping the following parameters fixed: $N_{\text{FFT}} = 16$, $B = 8$, $p = 13$, and $M = M_{\text{max}}$. We can observe that as we increase the embedding size, the loss decreases until we reach a certain point (which is dependent on the dataset). This is likely because a larger embedding size enables the model to capture more features; however, an excessively high embedding size may lead to overfitting.

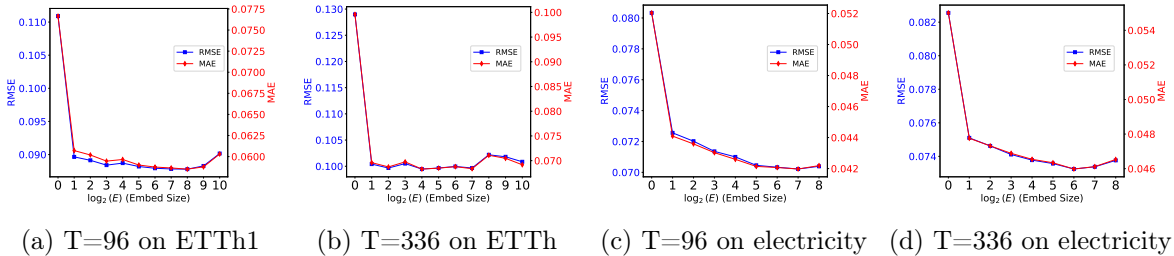


Figure 7: Comparison of MSE and MAE across different values of E for varying T on the ETTh1 and Electricity datasets.

Amount of Windows (High Dim) In this section, we evaluate the influence of the number of windows (p) on the model’s performance. We conducted experiments with different window counts $p \in \{3, 6, 14, 17, 25, 33\}$, while keeping the following parameters fixed: $B = 8$, $M = M_{\text{max}}$, and the overlap between windows is 50%.

FFT Resolution (N_{FFT}) In this section, we evaluate the influence of the FFT resolution (N_{FFT}) on the model’s performance. We conducted experiments with different $N_{\text{FFT}} \in$

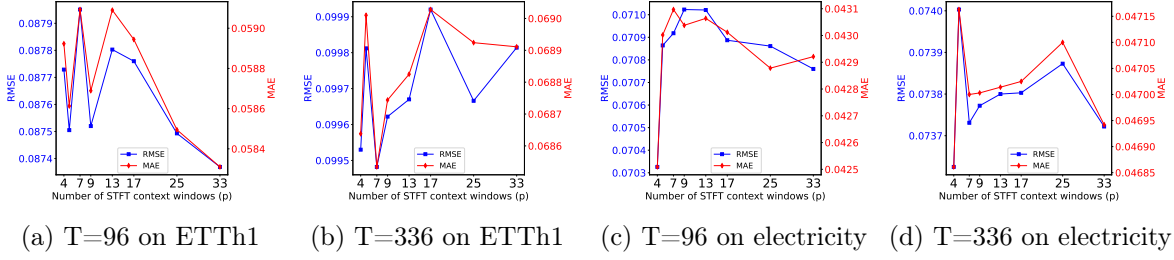


Figure 8: Comparison of MSE and MAE across different values of p for varying T on the ETTh1 and Electricity datasets.

$\{6, 8, 12, 16, 24, 32, 48\}$, while keeping the following parameters fixed: $p = 25$, $B = 8$, $M = M_{\max}$.

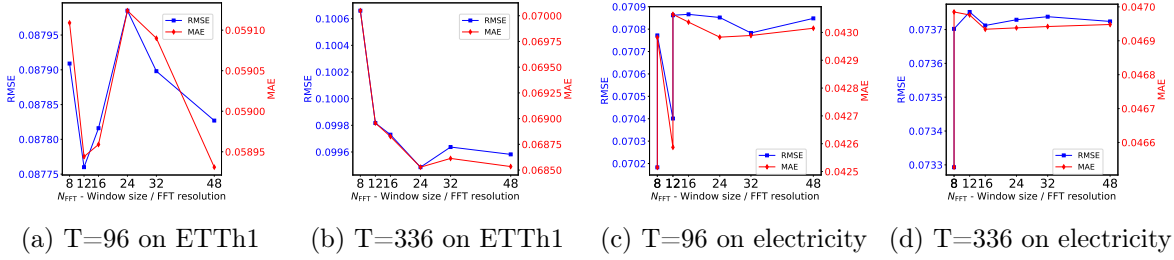


Figure 9: Comparison of MSE and MAE across different values of N_{FFT} for varying T on the ETTh1 and Electricity datasets.

Frequency Choose Max (M) In this section, we provide additional results for various datasets and prediction lengths T regarding the discussion on frequency compression 5.

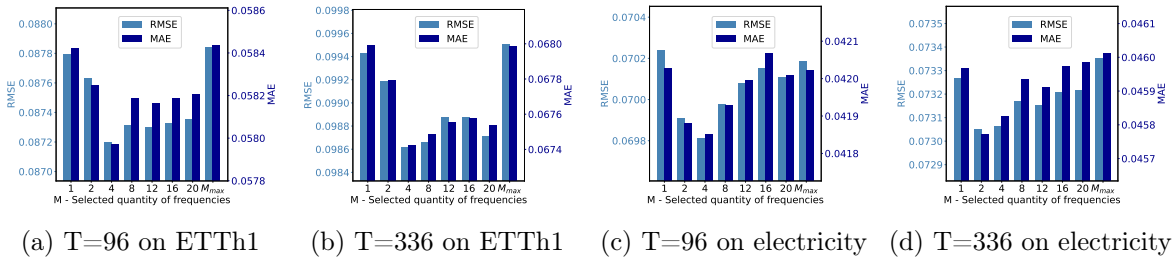


Figure 10: Comparison of MSE and MAE across different values of M for various T on the ETTh1 and Electricity datasets.

D.2 Different LookBack Window

In this section, we present additional results for various lookback windows on the ETTh1 and ETTm1 datasets.

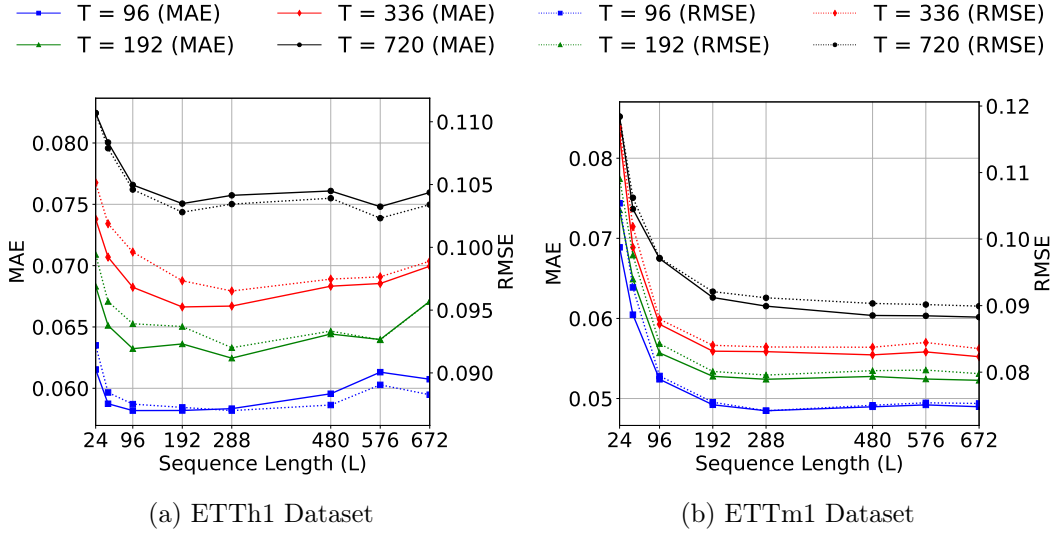


Figure 11: MAE and RMSE in relation to the Lookback Window L for varying prediction lengths $T \in \{96, 192, 336, 720\}$ for the ETTh1 and ETTm1 datasets.

D.3 Real Vs imaginary Components

This section provides additional information regarding the real versus imaginary experiment discussed in Section 5.3.3.

Dataset	I/O	96/96		96/192		96/336		96/720	
	Hidden Part	MAE	RMSE	MAE	RMSE	MAE	RMSE	MAE	RMSE
ETTh1	X^{Real}	0.0522	0.0797	0.0560	0.0850	0.0597	0.0888	0.0658	0.0958
	X^{Imag}	0.0521	0.0792	0.0562	0.0844	0.0592	0.0879	0.0684	0.0976
	W^{Real}	0.0522	0.0791	0.0557	0.0843	0.0588	0.0875	0.0669	0.0964
	W^{Imag}	0.0526	0.0801	0.0560	0.0849	0.0596	0.0888	0.0651	0.0953
	$W^{\text{Imag}}, X^{\text{Imag}}$	0.0523	0.0798	0.0560	0.0849	0.0592	0.0884	0.0644	0.0947
	$W^{\text{Real}}, X^{\text{Real}}$	0.0522	0.0791	0.0557	0.0843	0.0588	0.0887	0.0669	0.0930
	Normal	0.0522	0.0791	0.0565	0.0848	0.0592	0.0878	0.0685	0.0975
ETTm1	X^{Real}	0.0584	0.0877	0.0638	0.0944	0.0684	0.0997	0.0767	0.1047
	X^{Imag}	0.0582	0.0879	0.0634	0.0943	0.0679	0.0997	0.0756	0.1041
	W^{Real}	0.0586	0.0880	0.0644	0.0948	0.0685	0.0998	0.0759	0.1039
	W^{Imag}	0.0584	0.0880	0.0646	0.0951	0.0694	0.1008	0.0781	0.1065
	$W^{\text{Imag}}, X^{\text{Imag}}$	0.0586	0.0880	0.0644	0.0947	0.0685	0.0998	0.0759	0.1040
	$W^{\text{Real}}, X^{\text{Real}}$	0.0587	0.0882	0.0642	0.0948	0.0690	0.1005	0.0765	0.1050
	Normal	0.0586	0.0878	0.0639	0.0945	0.0684	0.0998	0.0765	0.1043

Table 8: Performance comparison on the ETTh1, ETTm1, and Electricity datasets for $I/O = 96 \times \{96, 192, 336, 720\}$ with different modes. X^{Real} and X^{Imag} refer to hiding the real and imaginary parts of the input, respectively. W^{Real} and W^{Imag} denote zeroing the real and imaginary weights, respectively. The cases where both the real and imaginary components are completely ignored (i.e., both weights and inputs are zeroed) are represented by $W^{\text{Imag}}, X^{\text{Imag}}$ and $W^{\text{Real}}, X^{\text{Real}}$. MAE and RMSE are reported, where lower values indicate better performance.

D.4 HC-MLP Experimental Results With For Various Values of p

In this section, we present additional results on the HC-MLP for various bases. Specifically, we provide results for the Quaternion base ($p = 2$, QuatMLP), Octonion base ($p = 4$, OctMLP), and Sedenion base ($p = 8$, SedMLP). Additionally, we include results for a model that aggregates all windows without using hyper-complex numbers, referred to as BasicMLP. Further details about its implementation can be found in B.3.

	Metric	Traffic				ETTh1				ETTm1			
		96	192	336	720	96	192	336	720	96	192	336	720
SedenionMLP ($p = 8$)	RMSE	0.0340	0.0346	0.0351	0.0363	0.0896	0.0948	0.0999	0.1047	0.0814	0.0857	0.0894	0.0977
	MAE	0.0168	0.0169	0.0173	0.0186	0.0598	0.0640	0.0685	0.0767	0.0542	0.0573	0.0609	0.0682
OctonionMLP ($p = 4$)	RMSE	0.0335	0.0343	0.0349	0.0361	0.0834	0.0874	0.0941	0.1017	0.0739	0.0831	0.0888	0.0967
	MAE	0.0166	0.0167	0.0172	0.0185	0.0579	0.0635	0.0676	0.0759	0.0496	0.0556	0.0603	0.0673
QuaternionMLP ($p = 2$)	RMSE	0.0335	0.0343	0.0350	0.0362	0.0874	0.0938	0.0997	0.1059	0.0796	0.0847	0.0887	0.0974
	MAE	0.0165	0.0167	0.0172	0.0184	0.0580	0.0633	0.0687	0.0783	0.0526	0.0564	0.0603	0.0678
BasicMLP	RMSE	0.0372	0.0391	0.0384	0.0415	0.0962	0.1025	0.1061	0.1187	0.0832	0.0903	0.0967	0.1066
	MAE	0.0180	0.0195	0.0201	0.0217	0.0650	0.0714	0.0761	0.0886	0.0546	0.0595	0.0649	0.0753

Table 9: Comparison of different hypercomplex structures on the ETT and Traffic datasets.

QuadMLP (2 windows), OctMLP (4 windows), and SedMLP (8 windows) represent hypercomplex models of increasing dimensionality, while BasicMLP is a non-hypercomplex linear model aggregating window information. Performance is reported using MSE and RMSE metrics, where lower values indicate better accuracy.

D.5 Extended Neighborhood Aggregation in WM-MLP

In this section, we present additional results on the WM-MLP with extended neighborhood aggregation. Specifically, we provide results for varying neighborhood sizes, where the model incorporates information not only from directly adjacent windows but also from second-order and third-order neighbors. The experiments were conducted on the ETTm1 and ETTh1 datasets with prediction lengths of 96, 192, 336, and 720.

For the two-neighbor case, the output C_i^{out} is computed as:

$$C_i^{\text{out}} = \sigma \left(C_i^{\text{in}} W_{i \rightarrow i} + C_{i-1}^{\text{in}} W_{(i-1) \rightarrow i} + C_{i+1}^{\text{in}} W_{(i+1) \rightarrow i} + C_{i-2}^{\text{in}} W_{(i-2) \rightarrow i} + C_{i+2}^{\text{in}} W_{(i+2) \rightarrow i} + B_i \right). \quad (7)$$

For the three-neighbor case, the output C_i^{out} is computed as:

$$C_i^{\text{out}} = \sigma \left(C_i^{\text{in}} W_{i \rightarrow i} + C_{i-1}^{\text{in}} W_{(i-1) \rightarrow i} + C_{i+1}^{\text{in}} W_{(i+1) \rightarrow i} + C_{i-2}^{\text{in}} W_{(i-2) \rightarrow i} + C_{i+2}^{\text{in}} W_{(i+2) \rightarrow i} + C_{i-3}^{\text{in}} W_{(i-3) \rightarrow i} + C_{i+3}^{\text{in}} W_{(i+3) \rightarrow i} + B_i \right). \quad (8)$$

	Metric	ETTh1				ETTm1			
		96	192	336	720	96	192	336	720
WM-MLP (1 Neighbor)	RMSE	0.084	0.088	0.097	0.102	0.076	0.082	0.089	0.094
	MAE	0.057	0.064	0.068	0.075	0.052	0.055	0.058	0.064
WM-MLP (2 Neighbors)	RMSE	0.084	0.087	0.095	0.100	0.074	0.080	0.087	0.092
	MAE	0.056	0.063	0.066	0.073	0.051	0.053	0.057	0.062
WM-MLP (3 Neighbors)	RMSE	0.084	0.087	0.095	0.101	0.075	0.080	0.087	0.094
	MAE	0.056	0.063	0.066	0.073	0.051	0.053	0.057	0.063

Table 10: Performance comparison of WM-MLP with varying numbers of neighbors (1, 2, and 3) on the ETTh1 and ETTm1 datasets for prediction lengths of 96, 192, 336, and 720. Metrics include RMSE and MAE. Results for WM-MLP with one neighbor are derived from the baseline values reported in the original paper.

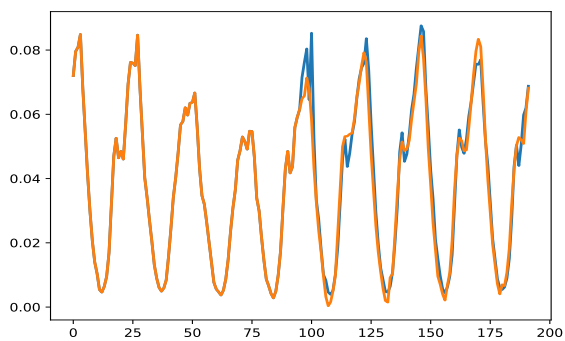
D.6 Complexity Analysis

We conducted an asymptotic analysis of modern models to compare their training time, memory usage, and testing steps. The results are summarized in Table 11. The comparison highlights the computational efficiency of the WM-MLP and HC-MLP models relative to other state-of-the-art approaches. Specifically, both models demonstrate competitive performance with logarithmic complexity in training time and memory, and a constant number of testing steps.

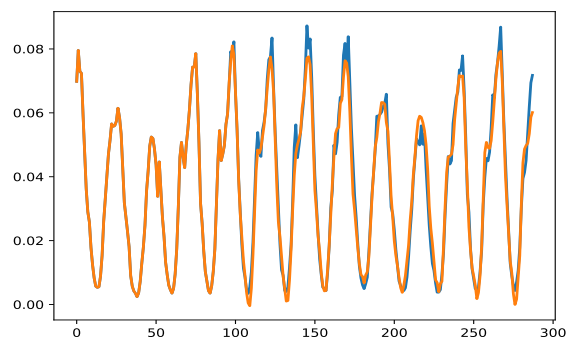
Method	Training Time	Training Memory	Testing Steps
WM-MLP	$\mathcal{O}(L \log \frac{L}{p})$	$\mathcal{O}(L)$	1
HC-MLP	$\mathcal{O}(L \log \frac{L}{p} + p^2)$	$\frac{1}{3}\mathcal{O}(L)$	1
FreTS	$\mathcal{O}(L \log L)$	$\mathcal{O}(L)$	1
PatchTST	$\mathcal{O}(L/S)$	$\mathcal{O}(L/S)$	1
LTSF-Linear	$\mathcal{O}(L)$	$\mathcal{O}(L)$	1
FEDformer	$\mathcal{O}(L)$	$\mathcal{O}(L)$	1
Autoformer	$\mathcal{O}(L \log L)$	$\mathcal{O}(L \log L)$	1
Informer	$\mathcal{O}(L \log L)$	$\mathcal{O}(L \log L)$	1
Transformer	$\mathcal{O}(L^2)$	$\mathcal{O}(L^2)$	L
Reformer	$\mathcal{O}(L \log L)$	$\mathcal{O}(L \log L)$	1

Table 11: Comparison of models in terms of asymptotic complexity for training time, memory usage, and testing steps as a function of the lookback window length (L). Here, S denotes the patch size used in PatchTST, and p represents the number of windows in the STFT transformation.

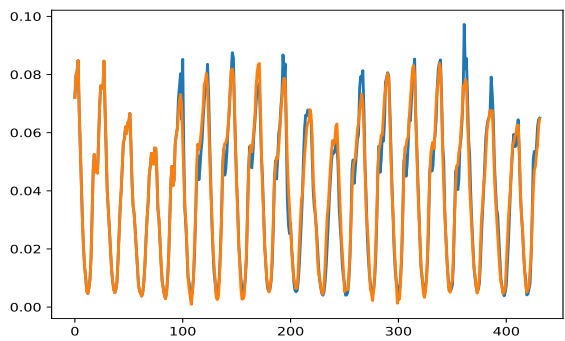
D.7 Visualizations



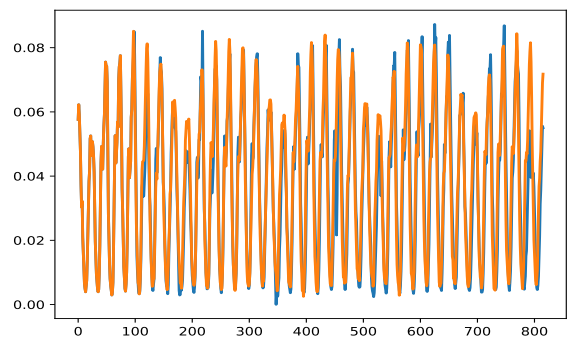
(a) Traffic I/O = 96/96



(b) Traffic I/O = 96/192

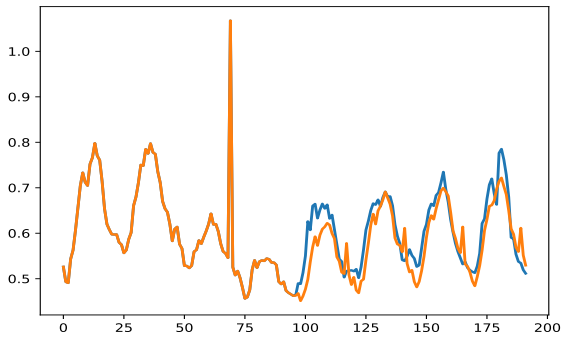


(c) Traffic I/O = 96/336

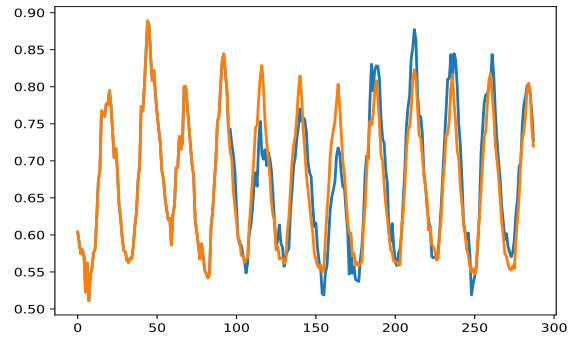


(d) Traffic I/O = 96/720

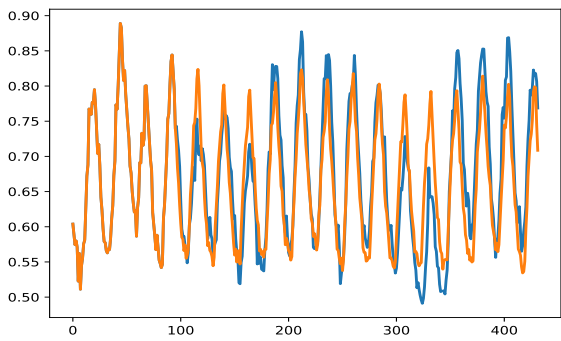
Figure 12: Ground Truth vs. Predictions for Different I/O Settings (Traffic Dataset).



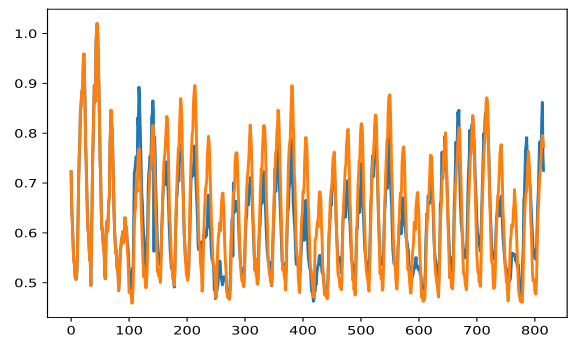
(a) Electricity I/O = 96/96



(b) Electricity I/O = 96/192



(c) Electricity I/O = 96/336



(d) Electricity I/O = 96/720

Figure 13: Ground Truth vs. Predictions for Different I/O Settings (Electricity Dataset).